Influence of ternary divalent cations (Mg^{2+}, Co^{2+}, Sr^{2+}) substitution on the physicochemical, mechanical and biological properties of carbonated hydroxyapatite scaffolds

Yanny Marliana B.I.[a]*, Muhammad Syazwan M.N.[a], Ahmad-Fauzi M.N.[a], Wendy B.[b], Yvonne R.[b],

[a] Biomaterials Niche Group, School of Materials & Mineral Resources Engineering, Engineering Campus, Universiti Sains Malaysia, 14300, Nibong Tebal, Penang, Malaysia.

[b] School of Science & Technology, Department of Engineering, Nottingham Trent University, Clifton Campus, Nottingham, NG11 8NS, United Kingdom.

* Corresponding author: Yanny Marliana Baba Ismail ; Tel.: +60 45996154

Email: yannymarliana@usm.my

Abstract

Substitution of ionic either anion or cation in a controlled amount into carbonated hydroxyapatite (CHA) structure is one of the efficient and safest ways in enhancing the properties of the materials. However, most of the works studied only focused on the physical and mechanical properties of single ionic substitution. For the first time, the influence of simultaneous ternary substitutions of divalent cations into porous CHA scaffolds on the physicochemical, mechanical, degradation and *in vitro* biological properties are investigated in the present study. Three different compositions of porous scaffolds with binary and ternary divalent cations, namely, pure CHA (S11), CoSr CHA (S21) and MgCoSr CHA (S31) were fabricated using polyurethane (PU) foam replication technique. Despite a small amount of Mg^{2+}, Co^{2+} and Sr^{2+} added, these divalent cations had successfully substituted into the Ca^{2+} site and remained as single phase B-type CHA. The produced scaffolds demonstrated open, interconnected and uniform pores. Interestingly, simultaneous ternary divalent cations substitution into CHA structure had successfully enhanced the compressive strength of the sintered scaffolds, also promoted better cell attachment and activities than the binary doped- and pure CHA scaffolds. It is important to note that the right choice of divalent cation can be the determining factor in tuning the physicochemical, mechanical and biological properties of CHA scaffolds.

Keywords: *Carbonated hydroxyapatite, Ternary doped, Divalent cation, Replication technique, Bone Scaffolds*

Introduction

Bone defects due to trauma or diseases resulted from sports/ road accidents and falls still pose a clinical challenge worldwide. As an alternative to autograft that has long been the gold standard in treating these defects, bone tissue engineering (BTE) using scaffold-based concept has been widely explored. An ideal bone scaffold should possess similar composition and architecture to human native bone. As such there are five essential characteristics to be fulfilled: (1) materials used and by-products should be non-toxic [1], (2) osteoconductive and osteoinductive by itself [2], [3], (3) resorbable/ degradable over time as new bone tissue forms [4], (4) interconnected pores with porosity (70-90%) and pore size (~200-500 µm) [5] and (5) sufficient mechanical strength to allow ease of handling [6].

Among various bioceramic materials, carbonated hydroxyapatite (CHA) ceramic has received considerable attention as scaffold material owing to its composition, which is more akin to the inorganic mineralized phase of human bone as compared to pure hydroxyapatite (HA). The amount of carbonate (CO_3^{2-}) found in bone mineral is about 2-8 wt% [3], [7]. It is well documented that CO_3^{2-} plays an essential role in enhancing bone metabolic activity [8]. The incorporation of CO_3^{2-} into HA offers better osteogenic behavior as compared to pure HA, which was observed by positive influence of CO_3^{2-} towards pre-osteoclastic and pre-osteoblastic cells responses during *in vitro* test [9]. Besides carbonate ions, various trace elements such as Mg^{2+}, Co^{2+}, Sr^{2+}, Zn^{2+}, Cu^{2+}, K^+ and Na^+ have attracted great interest to researchers due to the beneficial effects on bone repair and regeneration [10].

Among the trace elements, magnesium ions (Mg^{2+}) appear as one of the most abundant divalent ions present in human bone (0.6–0.7 wt%). Mg^{2+} plays an essential role in improving bone metabolism, particularly during the initial stage of osteogenesis as well as to stimulate rapid bone formation [11]. Moreover, *in vitro* study using human osteosarcoma cell lines (MG-63 cells) revealed that higher concentration of Mg^{2+} in HA, resulted in better cell attachment,
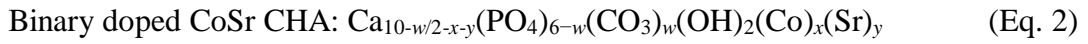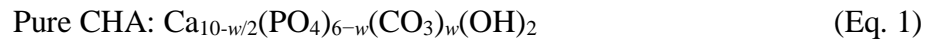
2

proliferation and differentiation compared to pure HA [12], [13]. The presence of Mg^{2+} was also reported to stimulate the proliferation of human endothelial cells [14]. Strontium ions (Sr^{2+}) has also attracted much attention in the synthesis of future bone materials. Despite the low concentration (0.01–0.02 wt%) detected in bone, Sr^{2+} is known to be the bone-seeking element. The incorporation of Sr^{2+} into HA structure has shown to accelerate the osteoblast and hinder osteoclast proliferations, resulting in rapid bone regeneration [15]. Cobalt (Co^{2+}) is another essential trace element found in human bone as an integral part in promoting angiogenesis. However, the amount of Co^{2+} added should be carefully controlled. For instance, the addition of high concentration of Co^{2+} above the safe limit (> 0.45 mM) into HA structure caused toxic effects to the biological surrounding once implanted into the patient's bodies [11]. While, the incorporation of small amount of Co^{2+} (5-12 wt%) into HA structure had encouraged angiogenesis demonstrated by the positive expression of vascular endothelial growth factor (VEGF) and erythropoietin (EPO) genes, which are the important indicators for neovascularization [16].

Among the fabrication techniques, polyurethane (PU) foam replication is one of the most common techniques to produce porous ceramic scaffolds with uniform interconnected pores, mimicking the structure of human cancellous bone. This simple technique allows a wide range of pore size distribution with high porosity and various shapes/sizes of scaffold can be produced economically [17]. However, previous studies had only focused on the pure and single doped HA scaffolds (i.e. Zn-HA, F-HA and CHA) produced by this particular technique [18]–[20]. To the best of our knowledge, the influence of ternary substitution of divalent cations into CHA porous sintered scaffolds is still lacking. Therefore, the aim of this study was to fabricate and characterize physically, chemically and mechanically the ternary divalent doped-CHA scaffolds prepared by PU foam replication technique followed by *in vitro* evaluation in determining the influence of these ions on the biocompatibility properties.

Experimental

Preparation of slurry and scaffolds

Pure, binary and ternary-doped CHA powders were prepared through nanoemulsion route at room temperature (27°C) following the procedure described in our previous work published elsewhere [21]. The compositions of the as-synthesized powders and molar concentration of reactants used are given in Table 1. The general empirical formulae for the as-synthesized powders are as follows:

$$\text{Pure CHA: } Ca_{10-w/2}(PO_4)_{6-w}(CO_3)_w(OH)_2 \qquad \text{(Eq. 1)}$$

$$\text{Binary doped CoSr CHA: } Ca_{10-w/2-x-y}(PO_4)_{6-w}(CO_3)_w(OH)_2(Co)_x(Sr)_y \qquad \text{(Eq. 2)}$$

$$\text{Ternary doped MgCoSr CHA: } Ca_{10-w/2-x-y-z}(PO_4)_{6-w}(CO_3)_w(OH)_2(Co)_x(Sr)_y(Mg)_z \quad \text{(Eq. 3)}$$

where, w = carbonate, x = cobalt, y = strontium, and z = magnesium ions.

Three-dimensional (3D) porous scaffolds were then fabricated by replication method using commercial polyurethane foams (PU, 60 ppi) impregnated in ceramic slurry. Initially, the as-synthesized powder (CHA, CoSrCHA or MgCoSrCHA) was mixed in deionized (DI) water with 5 wt% kaolin, a mixture of polyethylene glycol (PEG, M_w= 1500 g/mol, Fluka, Germany) and polyvinyl alcohol (PVA, M_w= 15 000 g/mol, Fluka, Germany) with a fixed ratio of 2:3, 5 wt% potassium carbonate (K_2CO_3, SYSTERM, Malaysia) and dispersant (Dispex A40) in preparing the ceramic slurry, as previously described in our work[20]. Small cubes of PU foam with dimensions of 15 mm (length) × 15 mm (width) × 15 mm (thickness) were soaked into the prepared ceramic slurry for 5 minutes to allow sufficient time for the impregnation. The coated foams were then carefully squeezed and released using two glass slides for 10 times in order to remove the excess slurry and prevent clogging of macropores inside the structure of the foam. The coated foams were subsequently vacuumed for 5 minutes, followed by drying in an oven at 60°C for 24 hours.

The dried foams were then sintered in an air atmosphere at 800°C using a chamber furnace (AWF-Laboratory Chamber Furnaces 1300°C, Lenton). Two-steps sintering were performed in producing the 3D CHA scaffolds. In the first stage, samples were slowly heated with a heating rate of 1°C/min to 500°C for 1 hour, followed by the second stage with continuous heating to 800°C at a rate of 5°C/min and soaked for 2 hours. During cooling stage at 250°C, the sintered scaffolds were removed from the furnace and immediately placed in a desiccator. Wet carbon dioxide (CO_2) gas was flowed into the desiccator with a rate of 0.5 L/min to recompensate the carbonate loss due to decarbonation. The samples were eventually left to cool for 24 hours in the desiccator before further characterizations.

Material characterizations

Phase analysis, crystallinity, lattice parameters and crystallite size of the sintered scaffolds were studied using X-ray Diffraction (XRD, D8 ADVANCE, Bruker) with Cu Kα radiation ($\lambda = 1.541$ Å), operating at 40 kV and 110 mA. Each diffraction scan was recorded in *2θ* range of 20˚ to 70˚ with a step size of 0.02˚. The obtained patterns were then matched with International Center for Diffraction Data (ICDD) with a file number of #09-0432, which referred to the HA standard reference pattern. The presence of functional groups and modes of carbonate substitution in the apatite structure were determined by Fourier Transform Infrared (FTIR) spectroscopy using a Perkin Elmer Spectrum One. Samples were prepared by mixing of the ground powders with potassium bromide (KBr) and pelletized using hand press at 5 MPa. Samples were scanned in transmittance mode (%T) from 400.00 to 4000.00 cm^{-1} with four scans per sample. The carbonate content of the sintered scaffolds was determined using Carbon Hydrogen Nitrogen (CHN) elemental analyzer (2400 Series II; Perkin-Elmer), where combustion of the sample was done over 950°C and the resulted gases such as carbon dioxide, water vapor and nitrogen oxides were detected. The amount of carbon (in wt%) obtained was multiplied by a factor of five, giving the percentage of carbonate (% of CO_3^{2-}) present.

The microstructure analysis of the pure, binary and ternary doped CHA scaffolds were observed under Tabletop Scanning Electron Microscope (SEM) (TM3000, Hitachi). Prior to imaging, all sintered scaffolds were coated with a thin layer of gold-palladium due to the poor electrical conductivity. The average pore sizes of the sintered scaffolds were then measured from the SEM micrograph using Image J^{TM} software (v1.50i.), in which 20 readings were taken for each composition. Sintered scaffolds were tested under compression using INSTRON 3369 universal tensile machine at a constant rate of 1.0 mm/min till fractured. The compression test was performed based on the procedure in ASTM C1424-04: Standard test method for advanced ceramics in terms of compressive strength at ambient temperature. Five scaffolds from each composition were subjected to load and mean compressive strength per scaffold was calculated. The results obtained were then plotted as mean ± standard deviation.

Biological studies

In vitro **bioactivity and degradation behavior**

Bioactivity and degradation tests of sintered scaffolds was carried out *in vitro* by immersing scaffolds in simulated body fluid (SBF) for different periods (7 and 14 days) with initial pH 7.4 at 37°C. The SBF was firstly, prepared according to Kukobo's recipe [22]. The ability of apatite formation on the sintered scaffolds after immersion in SBF solution were examined under Field Emission Scanning Electron Microscope (FESEM, Zeiss Supra 55VP) Meanwhile, the degradation of sintered scaffolds after immersion was monitored through weight loss (%) measurement. The changes in pH values of the SBF solution was also recorded at 7 and 14 days of immersion.

Cell culture

Human osteosarcoma cell lines (MG-63 cells) were used to assess the *in vitro* biocompatibility of the pure, binary and ternary doped CHA scaffolds (S11, S21 and S31). This test involved the study on cell viability, cell proliferation and early osteogenic differentiation of MG-63 cells in direct contact with the tested samples. Prior to cell seeding, the tested samples were sterilized in 1 ml of 70% industrial methylated spirit (IMS) for overnight followed by washed twice with phosphate-buffered saline (PBS).

MG-63 cells were expanded and cultured in standard 4.5 g/L high glucose Dulbecco's Modified Eagle Medium (DMEM), supplemented with 1% (v/v) L-glutamine (Lonza, United Kingdom), 1% (v/v) Penicilin-Streptomycin (Lonza, United Kingdom) and 10% (v/v) Fetal Bovine Serum (United Kingdom). 5×10^4 of MG-63 cells at passage 3 (P3) were seeded on the tested samples and incubated in a humidified atmosphere with 5% CO_2 at 37°C. Tissue culture plastic (TCP) was used as a positive control. Standard DMEM was used throughout the culture. Samples for both assays were collected on day 1 and 14. After the media were collected for each time point, cells were rinsed with PBS, trypsinized and stored in dH_2O at -80°C.

Cell viability

The biocompatibility of the tested samples was assessed firstly by observing the cell viability at day 1 and 3 using Live/Dead staining (Invitrogen, United Kingdom), which was prepared according to the manufacturer's instructions. Calcein-AM ester was used to fluorescently stain viable cells in green, while Propidium Iodide was used to label the nucleus of the dead cells in red. At each time-point, cell culture media was removed from tested samples followed by rinsed with 0.5 ml PBS staining solution containing 10 µM Calcein-AM and 1 µM Propidium Iodide and incubated for a period of 20 minutes. The samples were then rinsed once using 1ml PBS prior to observation under fluorescent microscope.

Cell proliferation

Cell proliferation was assessed by determining the level of total DNA released on day 1 and day 14. The level of DNA concentration of the tested samples were measured using PicoGreen® DNA quantification assay (Quant-iTTM PicoGreen® dsDNA assay kit, Invitrogen, United Kingdom). PicoGreen solution was prepared as 1: 200 dilutions in 1x Tris-EDTA (TE) buffer. DNA standard curve was prepared using the following concentrations (0-1 µg/ml). An equal volume of cell lysate or DNA standard to PicoGreen reagent was placed into each well of a 96 well plate. Samples were then incubated for 5 minutes in the dark, prior reading the fluorescence at 485/535 nm.

Alkaline phosphatase activity

Alkaline phosphatase (ALP) activity was used as a marker of early osteogenic differentiation. ALP activity was obtained from 4-Methylumbelliferyl phosphate, 4-MUP (Sigma-Aldrich, United Kingdom) reaction. Ranges of 4-Methylumbelliferone, 4-MU (Sigma-Aldrich, Switzerland) dilutions (0-2 µg/ml) were used to construct a standard curve. 50 µL of the cell lysate from each sample or standard of 4-MU and 50 µL of 4-MUP was then added into the relevant well of 96 well plate followed by incubation at 37°C for 90 minutes. To terminate the reaction, 100 µL of 1 X TE was added and the reading of the fluorescence was taken at 360/440 nm (excitation/emission).

Statistical Analysis

Statistical analyses were conducted to compare the levels of cell proliferation and osteogenic activity in response to different compositions of the tested samples. All data are reported as means ± standard deviation (SD). The statistical analyses were performed using GraphPad Prism software (version 7.0) by two-ways analysis of variance ANOVA conducted together with Tukey multiple comparison procedure. The significance level was set to *p*= 0.05.

A difference between the tested samples was considered to be significant at value of $p \leq 0.05$ (*), $p \leq 0.01$ (**), $p \leq 0.001$ (***), and $p \leq 0.0001$ (****). These biochemical assays were performed on $n = 3$ in duplicate and $n = 1$ for live/dead staining.

Results and Discussion

Scaffold characterization

The diffraction patterns of pure, binary and ternary doped CHA sintered scaffolds designated as S11, S21 and S31, respectively are shown in Fig. 1. The obtained diffraction peaks of all sintered scaffolds were indexed according to typical peaks of standard reference of HA (ICDD #09-0432) with a slight shift in peaks position to the lower diffraction angles. These peaks shift is due to the substitution of carbonate ions into the apatite structure, suggesting the phase form is single phase CHA even after being sintered at 800°C. In comparison with S11 scaffold, the diffraction patterns of S21 and S31 scaffolds have been continuously shifted (by a small degree) to lower 2θ angles, particularly the crystal planes in the region of $26° \leq (2\theta) \leq 35°$. This could be possibly attributed to the substitution of Mg^{2+}, Co^{2+} and Sr^{2+} into Ca^{2+} sites in the apatite structure as assumed earlier in empirical formulae.

Nine characteristic peaks were traced within the range $20° \leq (2\theta) \leq 70°$, with three broaden and overlapping peaks of (211), (112), (300) and (202) at $2\theta = 32$-$34°$. Other peaks of (002), (130), (222), (213) and (004) located at $2\theta = 26°$ and 40-$54°$, respectively, were also detected for all sintered scaffolds correspond to crystallographic planes of HA [23]. The peak of (112) at about $2\theta = 32°$, which usually appear in pure HA was also detected for all the sintered scaffolds. This indicated that small degree of decomposition of CHA phase had taken place during sintering. Previously, it has been reported in literature that decomposition of CO_3^{2-} from CHA structure begin at low temperature of 500-600°C when sintered in air. However,

there is no additional peaks correlated to the secondary phases such as $CaCO_3$ (ICDD #01-1032) and/or CaO (ICDD #03-0865) detected.

Interestingly, it is noticed that simultaneous substitution of Mg^{2+}, Co^{2+} and Sr^{2+} in CHA crystal structure had slightly reduced the degree of crystallinity. This is evidenced from the peaks broadening for S21 and S31 scaffolds, particularly at the overlapped peaks of (211), (112), (202) and (300) relative to S11 scaffold. It is also found that ternary substitution of divalent cations produced S31 scaffold with the smallest crystallite size as compared to S21 and S11 scaffolds. This could be assigned due to the competition between doped elements with different ionic radii, in which Mg^{2+} (0.71 Å), Co^{2+} (0.75 Å) and Sr^{2+} (1.13 Å) simultaneously substituted the Ca^{2+} sites (1.00 Å) into the apatite structure, which directly raises the crystal imperfection by the imposition of the structural disorder [24].

It is widely accepted that the substitution of CO_3^{2-} in the apatite crystal structure could alter the lattice parameters [25]. Most studies reported that the formation of B-type CHA could be described with the extension of *a*-axis and contraction of the *c*-axis, while the formation of A-type demonstrates the opposite effect [7], [26], [27]. However, in this work, all the sintered scaffolds showed increased in both *a* and *c*-axes simultaneously (Table 2). This can be explained due to the partial substitution of CO_3^{2-}, which mostly substituted into PO_4^{3-} sites (*c*-axis) with a small portion in Ca^{2+} (*a*-axis*)* sites for charge balance as shown in the empirical formulae assumed earlier in this work. Similar findings were reported earlier by Ivanova *et al.* [28] and Ezekiel *et al.* [29]. The rise in lattice parameters, particularly for *a*-axis also could be attributed to the partial substitutions of divalent cations simultaneously (Mg^{2+}, Co^{2+} and Sr^{2+}) into Ca^{2+} site in the apatite structure. Thus, the assumptions that the divalent cation dopants substitute into Ca^{2+} sites based on the empirical formulae (Eq. 2-3) are accepted.

The FTIR analysis of sintered scaffolds (Fig.2) is in good agreement with the previous XRD analysis. The FTIR spectra showed consistent trends of functional groups detection such

as CO_3^{2-}, PO_4^{3-} and OH^- groups which correspond to the characteristic bands of CHA. These confirmed that all the sintered scaffolds are B-type CHA, representing by the three main bands detected at 870-875 cm^{-1}, 1410-1430 and 1450-1470 cm^{-1} [30]. There are no bands of A-type CHA, which usually appears at about 880, 1500 and 1540-1545 cm^{-1} found [27], [31]. However, there is a minor change observed in the spectra of S21 and S31 scaffolds as compared to S11. The intensities of CO_3^{2-} band for S21 and S31 scaffolds were slightly decreased particularly at 870-875 cm^{-1} which explained the small degree of decomposition observed in the diffraction patterns. This gives us the indication that the carbonate content remained in S21 and S31 scaffolds are relatively lower than S11 scaffold, which will be later confirmed by CHN analysis.

Additionally, the FTIR spectra (Fig. 2) illustrated that all sintered scaffolds exhibited the characteristic bands located at about 465-475 cm^{-1} (v_2), 550-570 and 600-609 cm^{-1} (v_4), 960-966 cm^{-1} (v_1), and 1020-1120 cm^{-1} (v_3) are attributed to phosphate (PO_4^{3-}) groups in the apatite structure [30], [32]. The typical bands of the stretching modes for hydroxyl (OH^-) groups were detected at around 3400-3600 cm^{-1} (absorbed water) and 1600-1700 cm^{-1} (occluded water) [33], [34]. The results obtained thus far showed that there is no evidence of FTIR spectra disrupted with the addition of the controllable amount of divalent cation dopants (Mg^{2+}, Co^{2+} and Sr^{2+}) either in the binary or ternary CHA. This indicates that simultaneous substitution of a small amount of divalent cations into the apatite structure have no obvious effect on the total structure of CHA.

Among the sintered scaffolds, S11 scaffold has relatively higher carbonate content with 2.44 wt%, whereas, only 2.07 and 2.04 wt% of carbonate retained in S21 and S31 scaffolds, respectively. The trend is tally with the observation found in FTIR analysis (Fig. 2). Despite the loss of carbonate during sintering, the amount remained in all sintered scaffolds still fall in the range of carbonate presents in native human bone (2-8 wt%) [29], [35].

11

The sintering of pure, binary and ternary doped CHA scaffolds at 800°C resulted in highly porous structure with interconnected struts and open pores formation (Fig. 3). Despite the compositions, all sintered scaffolds exhibited basic structural features of uniform open pores of PU foam, with a 3D interpenetrating network of struts and pores. This could be attributed to the addition of binders (PEG:PVA) and kaolin which give a notable effect on the internal architecture of the sintered scaffolds. It is known that PEG act as a plasticizer to PVA and its role is to reduce the glass transition temperature (T_g) of the PVA. Subsequently, it enhances and maintains the flexibility of the scaffolds [36]. Meanwhile, kaolin is known to act as reinforcing agent in ceramic processing that could aids in forming a good bridging between the struts. This help to retain shape of the structure, indirectly strengthen the sintered scaffolds [37].

At the microscopic level, it can also be seen that the sintered scaffolds were able to achieve sufficient densification, particularly on the wall of struts. Particular attention should be paid to the addition of K_2CO_3 as sintering aid in the system that had improved the sinterability of CHA-based materials by accelerating the performance of densifying mechanism. Even with a small amount (5 wt%) of K_2CO_3 added, it appears favourable to provide sufficient densification of sintered scaffolds even though at low sintering temperature. This phenomenon is well correlated with the formation of liquid phase (melting of K_2CO_3) which fills in the gaps among the particles and creates a good bonding, thereby leading to fast diffusion rate during sintering [38]. However, plenty of cracks were found on the struts of the scaffold, particularly for S11 and S21 scaffolds in comparison to S31 scaffold. The existence of cracks on the struts is detrimental for porous scaffold as these flaws will be the point of failure that would contribute to further lower the strength of the scaffold. This observation suggested that the ternary substitution of divalent cations (Mg^{2+}, Co^{2+} and Sr^{2+}) could have played a role in encouraging better densification on the struts of the sintered scaffold with a minimal defect.

The pore size, porosity and compressive strength of pure, binary and ternary doped CHA scaffolds are presented in Table 3. Overall, the average pore sizes of different sintered scaffolds are in the range of 327-428 μm, which is appropriate for cells penetration, diffusion of nutrients and oxygen as well as removal of waste and carbon dioxide through the blood vessel (200-500 μm) [39]. The ideal pore size is one of a crucial characteristics in order to ensure the cells survival, particularly in the core of the scaffolds upon culture.

It is also noticed that there is a significant trend observed in the compressive strength of the sintered scaffolds, which associated with the influence of divalent cations incorporated into CHA crystal structure. It is expected that the simultaneous substitution of divalent cations, with addition of Mg^{2+}, Sr^{2+} and Co^{2+} could potentially enhance the mechanical properties of CHA-based materials. The trend obtained is also consistent with the SEM observation, where the features of internal architecture and physical appearance influenced towards enhancing the mechanical properties of the sintered scaffolds.

By comparing these sintered scaffolds, the maximum compressive strength of 0.53 ± 0.12 MPa was recorded for S31 scaffold, while S21 and S11 scaffolds showed the strength of 0.38 ± 0.04 MPa and 0.50 ± 0.05 MPa, respectively. It can be seen that S31 scaffold showed better mechanical strength, although it has a slight increase in total porosity (91.63%) as compared to S11 (89.61%) and S21 scaffolds (88.90%). This can be relates to the presence of Mg^{2+} in S31 scaffold. It is also believed that particle shape and size of the starting powder play important roles in improving the condition of the scaffolds structure. According to our previous work reported elsewhere [21], the incorporation of Mg^{2+} into the crystal structure promotes the formation of needle-like structures (MgCoSr CHA) as compared to the elongated and near spherical-like structures of CoSr CHA and CHA powders, correspondingly. This needle-like nanoparticles is thought to enhance the mechanical strength and toughness of MgCoSr CHA scaffolds. A similar observation has been reported by Kanchana and Sekar [40] where the

13

incorporation of Mg^{2+} into HA/β-TCP structure had exhibited high density and showed improvement in compressive strength, that is three times greater than the undoped HA/β-TCP composite. Overall, although the values are on the lower side, this compressive values for all sintered scaffolds are in the range of compressive strength of cancellous bone which is about 0.10-16.00 MPa [41]. Thus, the final products can be said to have potential as bone substitute material for non-loading applications.

In vitro bioactivity and degradation behavior

FESEM micrographs showed the formation of bone-like apatite on the surface of the pure, binary and ternary doped CHA scaffolds after 7 and 14 days of immersion in SBF solution (Fig.4.), indicating the *in vitro* bioactivity of scaffolds. At an early stage of immersion, it can be observed thin layer of apatite nucleation precipitates on the sintered scaffolds surface. Interestingly, the precipitates of the apatite crystals formed on the surface of the scaffolds showed different morphologies, which is thought to be due to the chemical compositions. With the prolonged of immersion time (14 days), the thin layer of apatite deposited on the surface had gradually grown into a larger amount and covered almost the entire surface. Among different compositions of scaffolds, the surface of S21 and S31 scaffolds showed rapid apatite formation, presented by deposition of the thick layer of the flower-like and granular-like morphologies, respectively. It is believed that the incorporation of ternary divalent cations (Mg^{2+}, Co^{2+} and Sr^{2+}) into the structure have a significant role towards improving biological properties.

The *in vitro* biodegradation of pure, binary and ternary doped CHA scaffolds after immersion in SBF solution for 14 days is shown in Fig. 5. The trend illustrates the increased in weight loss of all sintered CHA scaffolds with prolonged in immersion time. S21 scaffolds showed relatively higher weight loss (2.41%) after 14 days of immersion as compared to S11

scaffold. This suggests that the simultaneous substitution of divalent cations into the apatite structure, resulting in higher solubility than CHA alone (S11 scaffold). However, between the divalent doped CHA scaffolds, it can be seen that S31 scaffold has slightly lower weight loss at both time-points. This indicated that the presence of Mg^{2+} into S31 structure was found to be able to control the degradation of the divalent doped CHA scaffold. A similar observation had been reported earlier where the substitution of Mg^{2+} in Ca-silicates could potentially reduce their degradation rate as well as enhance the mechanical properties [42]

The pH value of the SBF solution (physiological environment) has direct correlation with the degradation and apatite deposition on the surface that occur during immersion time. The general trend of pH values of SBF solution for S21 and S31 scaffolds increased during the initial time of immersion and gradually decreased after 14 days as demonstrated in Fig. 5. In comparison to S11 scaffold, the pH values of S21 and S31 scaffolds were found to be in the range of 7.42-7.93, which is slightly higher than the normal pH of SBF of about 7.4. This phenomenon can be explained by cationic exchanges that involved doping elements (Mg^{2+}, Co^{2+} and Sr^{2+}) as well as Ca^{2+} that occurred between the surface of the scaffolds and the SBF solution, resulting in the formation of apatite layer. The variation of pH results is tally with the weight loss as described.

Assessment of biocompatibility

The morphology, attachment and viability of MG-63 cells seeded on the tested samples were observed under fluorescent microscope at different time points (Fig. 6). Overall, MG-63 cells were able to attach and proliferate throughout the entire surface over time, indicating good biocompatibility of the tested samples. Initial cell attachment is an essential indicator of biocompatibility and determinant of the potential of the material in supporting further cell activities including proliferation and differentiation [43], [44]. In addition, cells in direct contact

15

with pure, binary and ternary-doped CHA scaffolds demonstrated elongated fibroblasts-like morphology, which is consistent with the control sample at both time-points.

Among the tested compositions, S21 showed the least population of viable cells relative to the control. Although the morphology of the cells is nearly the same, higher population of dead cells were observed when the cells were in direct contact with S21 even at day 1 of culture. This may be due to high ion released from S21 into the culture media, which had changed the pH (slightly above pH 8) and color of the media to orangey red (data not shown for brevity). It is believed that this rapid released of Co^{2+} and Sr^{2+} from S21 in high proportions at the early stage of culture had adversely affected the cell viability, which resulted in significant number of cells death. As a consequence, only a small number of cells survived and proliferated on S21 over time. While, cells cultured on S11 and S31 exhibited higher population of viable cells and found to be well spread in comparison to S21. The addition of Mg^{2+} together with Co^{2+} and Sr^{2+} forming the ternary CHA compositions had helped in controlling the ions released into the culture media as compared to S21. Cells cultured on both S11 and S31 also showed the normal color of culture media and pH (between pH 7-7.4).

The proliferation of MG-63 cells on pure, binary and ternary doped CHA tested samples was estimated by their level of DNA released after 1 and 14 days (Fig. 7). The proliferation of MG-63 cells cultured on all tested samples increased gradually from day 1 to day 14. This is consistent with the observation on the cell viability, which corresponds to the number of viable cells. At early time-point, cell cultured on all tested samples demonstrated a relatively lower level of DNA concentration in comparison to TCP control ($p \leq 0.0001$). Among all the tested samples, the highest DNA concentration was recorded for S11, followed by S31 and S21 powders at day 1 ($p \leq 0.005$ and $p \leq 0.0001$, respectively). By prolonging the culture period to 14 days, S31 over performed represented by significant increase in the DNA concentration as compared to S21 ($p = 0.003$) and S11 ($p \leq 0.0001$). This highlighted that the ternary

16

substitutions of the divalent cations (Mg^{2+}, Co^{2+} and Sr^{2+}) into the apatite structure had enhanced the cell proliferation as compared to S11. Hence, the presence of controlled amount of dopants in the CHA lattice could be beneficial for cell attachment, viability and proliferation without causing any toxicity effects to the cells.

The early osteogenic differentiation of MG-63 cells was quantified based on the alkaline phosphatase (ALP) activity on pure, binary and ternary doped CHA tested samples. The level of ALP/DNA obtained for all tested samples represented a time-dependent pattern, where the pattern was gradually increased over time (Fig. 8). Despite of the compositions, S11, S21 and S31 samples showed higher level of mean ALP/DNA at the early period of culture as compared to TCP control ($p = 0.3041$, $p = 0.1869$ and $p = 0.0361$, respectively), but no significant differences were observed between them. At day 14, cells in direct contact with S21 showed the lowest level of mean ALP/DNA. While, cell cultured on S31 revealed significantly higher level of mean ALP/DNA relative to S21 ($p = 0.0063$) and S11 ($p = 0.0140$). It is believed that the substitution of Mg^{2+} into CHA structure together with Co^{2+} and Sr^{2+} was found to be more favorable in enhancing osteogenic differentiation of MG63-cells, compared to Mg-free counterparts. A similar observation was reported by Fiocco *et.al.* who showed that the incorporation of Mg in Ca-silicates system play a significant role in enhancing the osteogenic differentiation and matrix production of MC3T3-E1 cells cultured on highly porous Ca-Mg silicate ceramic scaffolds [42].

Conclusion

- Pure, binary and ternary-doped CHA ceramics were successfully synthesized as highly porous scaffolds by PU foam replication technique at low sintering temperature.
- After ceramisation, the fabricated scaffolds possess single phase B-type CHA with sufficient amount of carbonate in the apatite structure and exhibited

interconnected open pore structure with about 90% porosity, pores size of 327- 428 μm and compressive strength of 0.38-0.53 MPa depending on their compositions.

- The addition of Mg^{2+} conjugated with Co^{2+} and Sr^{2+} forming the ternary-doped CHA scaffolds had benefited both the architecture and mechanical properties by the formation of densified and more uniform struts.

- None of the tested compositions are considered toxic to MG-63 cells. However, binary-doped CHA composition was found to be the least favorable for cell attachment and activity due to abrupt ion released during early stage of culture indicated by changes in pH and color of culture media. Interestingly, the presence of Mg^{2+} in ternary-doped CHA had enhanced the biocompatibility properties.

- This work highlights that the right choice of divalent cations doped simultaneously into CHA structure would greatly influenced the final properties of the scaffolds.

- Future studies on the influence of ion releases on bone cells and its surrounding cells particularly endothelial and immune cells would provide a better understanding in designing a novel osteoimmunomodulated scaffolds.

Conflict of Interest

The authors declare no conflict of interest.

Acknowledgements

References

[1]   Salgado A. J., Coutinho O. P., & Reis R. L.: Bone tissue engineering: state of the art and future trends. *Macromol. Biosci.* 4 (8), 743-765 (2004).

[2]   Siddiquee S. *Composite Materials: Applications in Engineering, Biomedicine and Food Science.* Springer Nature. (2020)

[3]   Mediaswanti K., Wen C., Ivanova E.P., Berndt C.C., Malherbe F., Pham V. and Wang J.: A Review on Bioactive Porous Metallic Biomaterials. *J. Biomim. Biomater. Tissue Eng.* 18 (1), 2–8 (2013)

[4]   Yanny Marliana B.I., Ferreira A. M., Bretcanu O., Dalgarno K., & El Haj A. J.: Polyelectrolyte multi-layers assembly of SiCHA nanopowders and collagen type I on aminolysed PLA films to enhance cell-material interactions. *Colloids Surf. B: Biointerfaces.* 159, 445-453 (2017)

[5]   Tajbakhsh S. and Hajiali F.: A comprehensive study on the fabrication and properties of biocomposites of poly(lactic acid)/ceramics for bone tissue engineering. *Mater. Sci. Eng. C.* 70, 897–912 (2016)

[6]   Fiume E., Barberi J., Verné E. and Baino F.: Bioactive Glasses : From Parent 45S5 Composition to Scaffold-Assisted Tissue-Healing Therapies. *J. Func. Biomater.* 9 (1), 24 (2018)

[7]   Yanny Marliana B.I., Wimpenny I., Bretcanu O., Dalgarno K., & El Haj, A. J.: Development of multisubstituted hydroxyapatite nanopowders as biomedical materials for bone tissue engineering applications. *J. Biomed. Mater. Res. A.* 105 (6), 1775-1785 (2017)

[8]   Li S. Yu W., Zhang W., Zhang G., Yu L., & Lu E.: Evaluation of highly carbonated hydroxyapatite bioceramic implant coatings with hierarchical micro-/nanorod topography optimized for osseointegration. *Int. J. Nanomedicine.* 13, 3643 (2018)

[9]   Germaini M. M., Detsch R., Grünewald A., Magnaudeix A., Lalloue F., Boccaccini A. R., & Champion E.: Osteoblast and osteoclast responses to A/B type carbonate-substituted hydroxyapatite ceramics for bone regeneration. *Biomed. Mater.* 12 (3), 035008 (2017)

[10]   Kulanthaivel S., Roy B., Agarwal, T., Giri S., Pramanik K., Pal K., Ray S.S., Maiti T.K. and Banerjee I.: Cobalt doped proangiogenic hydroxyapatite for bone tissue engineering application. *Mater. Sci. Eng. C.* 58, 648–65 (2016)

[11]   Kulanthaivel S., Mishra U., Agarwal T., Giri S., Pal K., Pramanik K. and Banerjee I.: Improving the osteogenic and angiogenic properties of synthetic hydroxyapatite by dual doping of bivalent cobalt and magnesium ion. *Ceram. Int.* 41 (9), 11323–11333 (2015)

[12]   Geng Z., Wang R., Li Z., Cui Z., Zhu S., Liang Y., Liu Y., Huijing B., Li X., Huo Q. and Liu Z.: Synthesis, characterization and biological evaluation of strontium/magnesium-co-substituted hydroxyapatite. *J. Biomater. Appl.* 31 (1), 140-151 (2016)

[13]   Szurkowska K., Zgadzaj A., Kuras M., & Kolmas J.: Novel hybrid material based on Mg^{2+} and SiO_4^{4-} co-substituted nano-hydroxyapatite, alginate and chondroitin sulphate for potential use in biomaterials engineering. *Ceram. Int.* 44 (15), 18551–18559 (2018)

[14] Bose S., Fielding G., Tarafder S., & Bandyopadhyay A.: Understanding of dopant-induced osteogenesis and angiogenesis in calcium phosphate ceramics. *Trends Biotechnol.* 31 (10), 594–605 (2013)

[15] Lowry N., Han Y., Meenan B. J., & Boyd A. R.: Strontium and zinc co-substituted nanophase hydroxyapatite. *Ceram. Inter.* 43 (15), 12070-12078 (2017)

[16] Ignjatovic N., Ajdukovic Z., Rajkovic J., Najman S., Mihailovic D., & Uskokovic D.: Enhanced Osteogenesis of Nanosized Cobalt-substituted Hydroxyapatite. *J. Bionic Eng.* 12 (4), 604–612 (2015)

[17] Da Mota, M., De, V. and Branco, A.: Polyurethane-based Scaffolds for Bone Tissue Regeneration, PhD Thesis. Instituto Superior Técnico. (2015)

[18] Batra U. and Kapoor S.: Ionic Substituted Hydroxyapatite Scaffolds Prepared by Sponge Replication Technique for Bone Regeneration. *J. Nanosci. Nanotechno.* 6, 18–24 (2016)

[19] Fook A. C. B. M., Aparecida A. H., Fideles T. B., Costa R. C., & Fook M. V. L.: Porous hydroxyapatite scaffolds by polymer sponge method. *Key Eng. Mater* 396-398, 703-706 (2009)

[20] Muhammad Syazwan M. N., Ahmad-Fauzi, M. N., Balestri, W., Reinwald, Y., & Yanny Marliana B. I.: Effectiveness of various sintering aids on the densification and in vitro properties of carbonated hydroxyapatite porous scaffolds produced by foam replication technique. *Mater. Today Commun.* 27, 102395 (2021)

[21] Muhammad Syazwan M.N. and Yanny Marliana B.I.: The influence of simultaneous divalent cations (Mg^{2+}, Co^{2+} and Sr^{2+}) substitution on the physico-chemical properties of carbonated hydroxyapatite. *Ceram. Int*. 45 (12) 14783-14788 (2019)

[22] Kokubo T., & Takadama H.: How useful is SBF in predicting in vivo bone bioactivity?. *Biomaterials*. 27 (15), 2907-2915 (2006)

[23] Xue C., Chen Y., Huang Y. and Zhu P.: Hydrothermal Synthesis and Biocompatibility Study of Highly Crystalline Carbonated Hydroxyapatite Nanorods. *Nanoscale Res. Lett.* 10 (1), 1–6 (2015)

[24] Avci M., Yilmaz B., Tezcaner A., & Evis Z.: Strontium doped hydroxyapatite biomimetic coatings on Ti_6Al_4V plates. *Ceram. Int.* 43 (12) 9431–9436 (2017)

[25] Kamitakahara M., Nagamori T., Yokoi T. and Ioku K.: Carbonate-containing hydroxyapatite synthesized by the hydrothermal treatment of different calcium carbonates in a phosphate-containing solution. *J. Asian Ceram. Soc.* 3 (3), 287–291 (2015)

[26] Yang W. H., Xi X. F., Li J. F., & Cai K. Y.: Comparison of crystal structure between carbonated hydroxyapatite and natural bone apatite with theoretical calculation. *Asian J. Chem.* 25 (7), 3673–3678 (2013)

[27] Šupová M.: Substituted hydroxyapatites for biomedical applications: A review. *Ceram. Int.* 41 (8), 9203-9231 (2015)

[28] Ivanova T. I., Frank-Kamenetskaya O. V., Kol'tsov A. B. and Ugolkov V. L.: Crystal Structure of Calcium-Deficient Carbonated Hydroxyapatite. Thermal Decomposition, *J. Solid State Chem.* 160 (2) 340–349 (2001)

[29]   Ezekiel I., Kasim S. R., Yanny Marliana B.I., and Ahmad-Fauzi M.N.: Nanoemulsion synthesis of carbonated hydroxyapatite nanopowders : Effect of variant CO_3^{2-} / PO_4^{3-} molar ratios on phase, morphology, and bioactivity. *Ceram. Int.* 44 (11), 13082–13089 (2018)

[30]   Youness R. A., Taha M. A., Elhaes H., & Ibrahim M.: Molecular modeling, FTIR spectral characterization and mechanical properties of carbonated-hydroxyapatite prepared by mechanochemical synthesis. *Mater. Chem. Phys.* 190, 209-218 (2017)

[31]   Lala S., Ghosh M., Das P. K., Das D., Kar T., & Pradhan S. K.: Magnesium substitution in carbonated hydroxyapatite: structural and microstructural characterization by Rietveld's refinement. *Mater. Chem. Phys.* 170, 319-329 (2016)

[32]   Garskaite E., Gross K.A., Yang S.W., Yang T.C.K., Yang J.C. and Kareiva A.: Effect of processing conditions on the crystallinity and structure of carbonated calcium hydroxyapatite (CHAp). *CrystEngComm.* 16 (19), 3950-3959 (2014)

[33]   Hazar Yoruc, A. B., Karakaş, A., Ayas, E., & Koyun, A.: Effect of precipitation method on properties of hydroxyapatite powders. *Acta Phys. Pol. A.* 123 (2), 371–373 (2013)

[34]   Reem A. W., Jafer R., Yahia I. S., Al-Ghamdi A. A., Al-ghamdi M. A., & El-Naggar A. M.: Fast and easy synthesis of novel Strontium apatite nanostructured phase: Structure, spectroscopy, and dielectric analysis. *Ceram. Int.* 43 (18), 17153-17159 (2017)

[35]   Safarzadeh M., Ramesh S., Tan C.Y., Chandran H., Ching Y.C., Ahmad-Fauzi M.N., Krishnasamy S. and Teng W.D.: Sintering behaviour of carbonated hydroxyapatite prepared at different carbonate and phosphate ratios. *Bol. Soc. Esp. Cerám. V.* (2019)

[36]   McKeen L.W.: Used in Medical Devices, *Handb. Polym. Appl. Med. Med. Devices. Elsevier Inc.* 21–53 (2014)

[37]   Settanni G., Zhou J., Suo T., Schöttler S., Landfester K., Schmid F. and Mailänder V.: Protein corona composition of PEGylated nanoparticles correlates strongly with amino acid composition of protein surface. *arXiv preprint arXiv* 1612.08814 (2016)

[38]   German R.M., Suri P. and Park S.J.: Review : liquid phase sintering. *J. Mater. Sci.* 44 (1), 1–39 (2009)

[39]   Saba G., Hesaraki S., and Hajisafari M.: Utlization of rheological parameters for the prediction of β-TCP suspension suitability to fabricate bone tissue engineering scaffold through foam replication method. *J. Aust. Ceram. Soc.* 54 (4), 587–599 (2018)

[40]   Kanchana P. and Sekar C.: Effect of magnesium on the mechanical and bioactive properties of biphasic calcium phosphate. *J. Miner. Mater. Charac. Engine.* 11 (10), 982 (2012)

[41]   Gerhardt L.C. and Boccaccini A.R.: Bioactive glass and glass-ceramic scaffolds for bone tissue engineering. *Materials.* 3 (7), 3867-3910 (2010)

[42]   Fiocco L., Li S., Stevens M. M., Bernardo E., & Jones J. R.: Biocompatibility and bioactivity of porous polymer-derived Ca-Mg silicate ceramics. *Acta Biomater.*, 50, 56-67 (2017)

[43]   Zhou J. and Zhao L.: Multifunction Sr, Co and F co-doped microporous coating on titanium of antibacterial, angiogenic and osteogenic activities. *Sci. Rep.* 6 (1), 29069 (2016)

[44] Ahmed M.K., Mansour S.F., Al-Wafi R., Afifi M. and Uskoković V., Gold as a dopant in selenium-containing carbonated hydroxyapatite fi llers of nano fi brous ε - polycaprolactone sca ff olds for tissue engineering. *Int. J. Pharm*. 577, 118950 (2020)

LIST OF FIGURE CAPTIONS

Fig. 1 Diffraction patterns of pure, binary and ternary doped CHA sintered scaffolds (a) S11, (b) S21 and (c) S31

Fig. 2 FTIR spectra of pure, binary and ternary doped CHA sintered scaffolds in comparison to control CHA, (a) S11, (b) S21 and (c) S31. Green dotted line refers to OH^- group, blue represent CO_3^{2-} group and red line is PO_4^{3-} group

Fig. 3 Micropores structure of the pure, binary and ternary doped CHA scaffolds at 800°C, (a) S11, (b) S21 and (c) S31 sintered scaffolds (red arrow marks the crack on struts). Scale bar = 1 mm, magnification of 60 X

Fig. 4 FESEM micrographs of the surface of the immersed pure, binary and ternary doped CHA scaffolds after 7 and 14 days in simulated body fluid. Scale bar = 1 μm, magnification of 10 K X

Fig. 5 pH value and weight loss of pure, binary and ternary doped CHA scaffolds after immersion in SBF solution for 14 days

Fig. 6 Cell viability of MG-63 cells seeded on the TCP control, S11, S21 and S31 after 1 and 3 days in culture. Green fluorescent signal represents the viable cells and red fluorescent stain shows the nucleus of dead cells. Scale bar = 100 μm

Fig. 7 Cell proliferation of MG-63 cells on pure, binary and ternary doped CHA tested samples were assessed by DNA concentration after 1 and 14 days in comparison with control. Value represent the mean $\pm$ SD of three samples duplicate (*$p \leq 0.05$, **$p \leq 0.01$, ***$p \leq 0.001$ and **** $p \leq 0.0001$). Cells in direct contact with S31 show highest level of DNA after 14 days of culture

Fig. 8 The level of mean ALP/DNA by MG-63 cells cultured on control, pure, binary and ternary doped CHA tested samples for 1 and 14 days. Value represent the mean $\pm$ SD of three samples duplicate (*$p \leq 0.05$, **$p \leq 0.01$, ***$p \leq 0.001$ and **** $p \leq 0.0001$). Cells in direct contact with S31 show highest level of mean ALP/DNA after 14 days of culture

LIST OF TABLE CAPTIONS

Table 1 Compositions of the as-synthesized CHA and multi-doped CHA powders

Table 2 Crystallographic features of pure, binary and ternary doped CHA sintered scaffolds

Table 3 Pore size, porosity and compressive strength of pure, binary and ternary doped CHA scaffolds
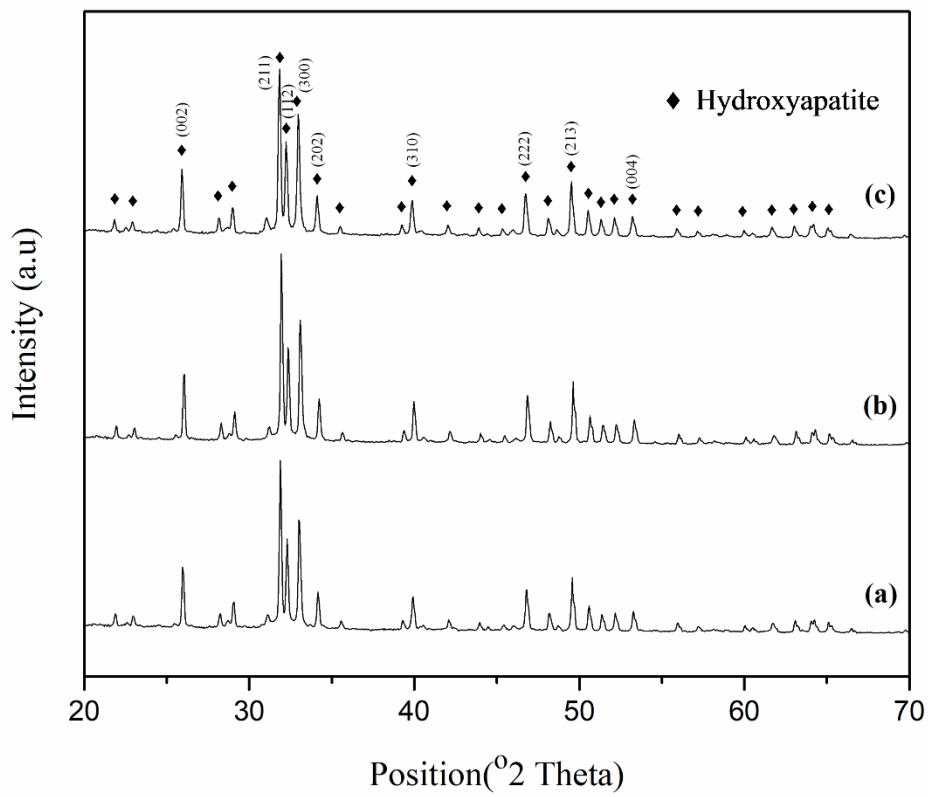
LIST OF FIGURES

Fig. 1 Diffraction patterns of pure, binary and ternary doped CHA sintered scaffolds (a) S11, (b) S21 and (c) S31
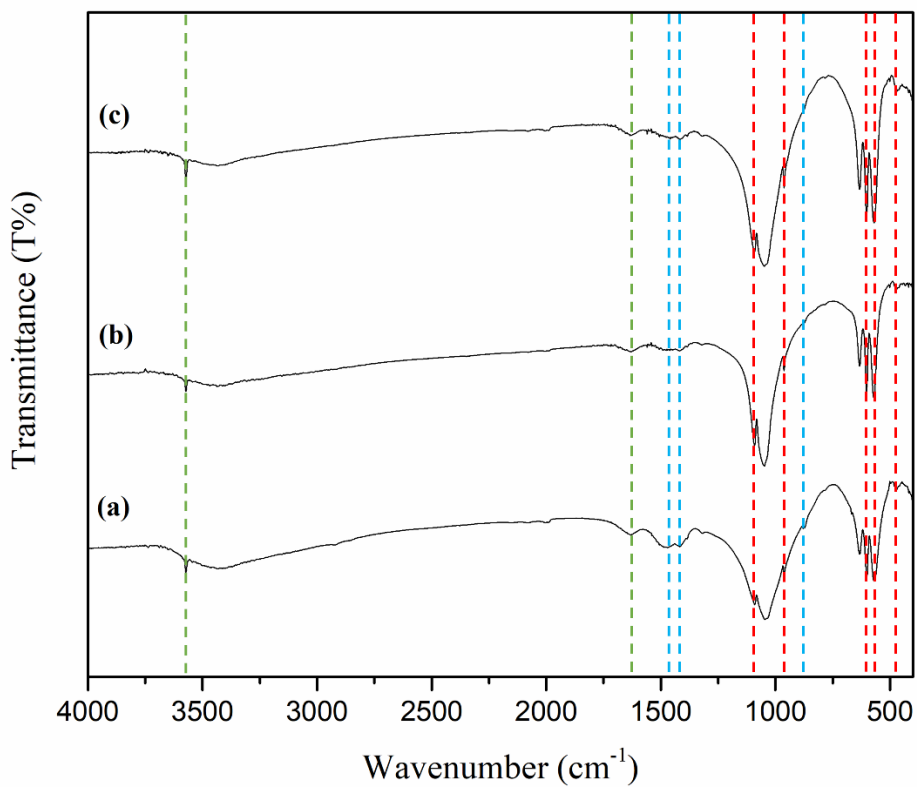
Fig. 2 FTIR spectra of pure, binary and ternary doped CHA sintered scaffolds in comparison to control CHA, (a) S11, (b) S21 and (c) S31. Green dotted line refers to OH$^-$ group, blue represent CO_3^{2-} group and red line is PO_4^{3-} group
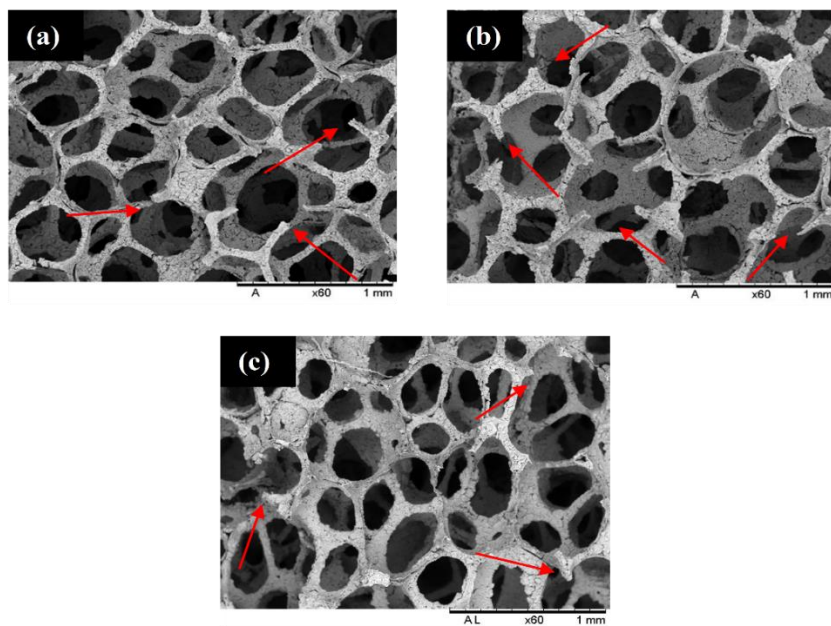
Fig. 3 Micropores structure of the pure, binary and ternary doped CHA scaffolds at 800°C, (a) S11, (b) S21 and (c) S31 sintered scaffolds (red arrow marks the crack on struts). Scale bar = 1 mm, magnification of 60 X

Samples	Days		
	0	**7**	**14**
S11			
S21			
S31			

Fig. 4 FESEM micrographs of the surface of the immersed pure, binary and ternary doped CHA scaffolds after 7 and 14 days in simulated body fluid. Scale bar = 1 μm, magnification of 10 K X
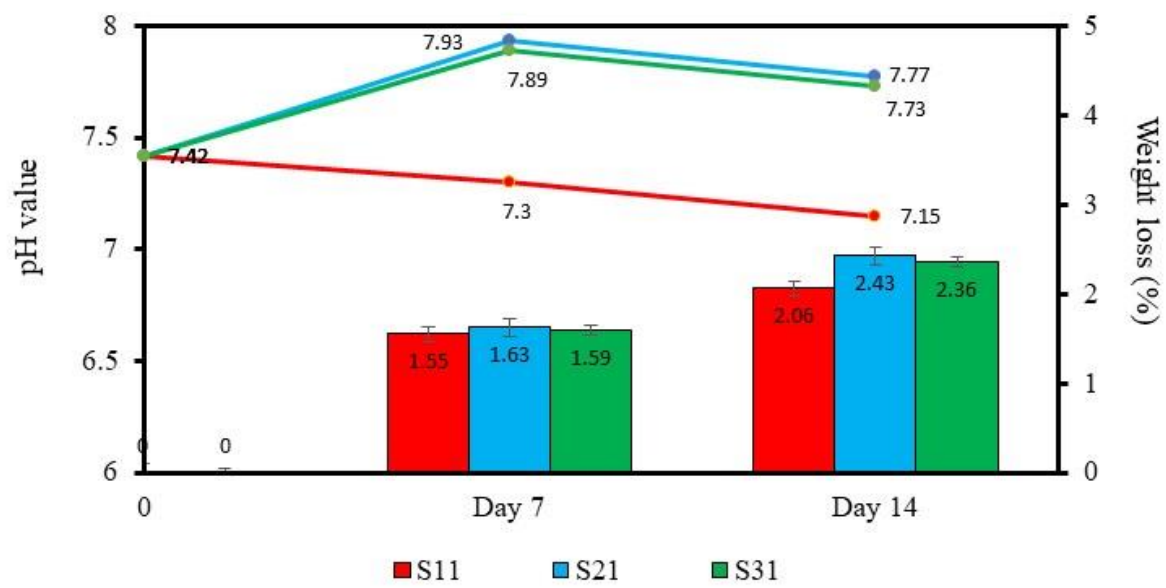
26

Fig. 5 pH value and weight loss of pure, binary and ternary doped CHA scaffolds after immersion in SBF solution for 14 day

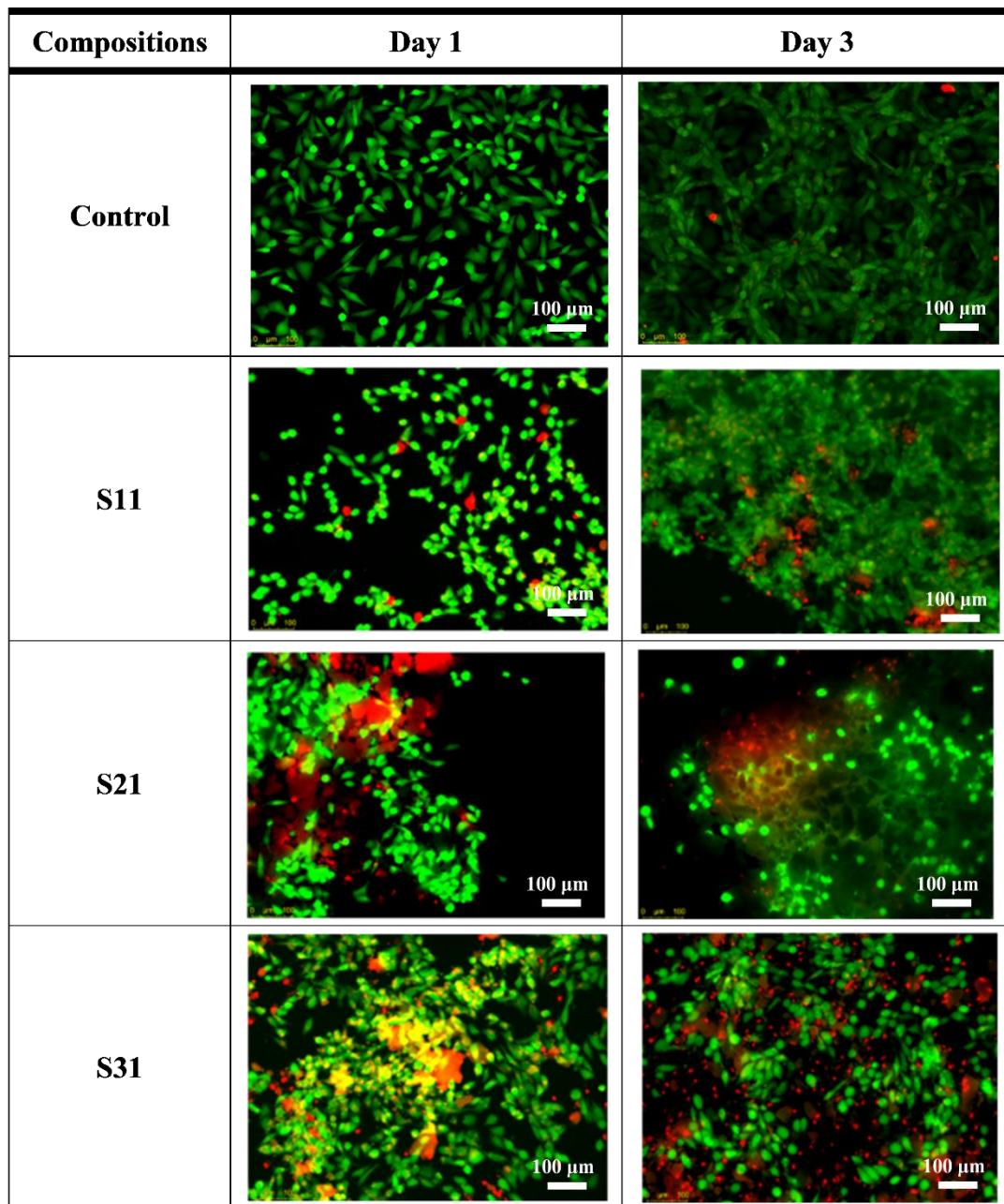| Compositions	Day 1	Day 3
Control		
S11		
S21		
S31		

Fig. 6 Cell viability of MG-63 cells seeded on the TCP control, S11, S21 and S31 after 1 and 3 days in culture. Green fluorescent signal represents the viable cells and red fluorescent stain shows the nucleus of dead cells. Scale bar = 100 μm
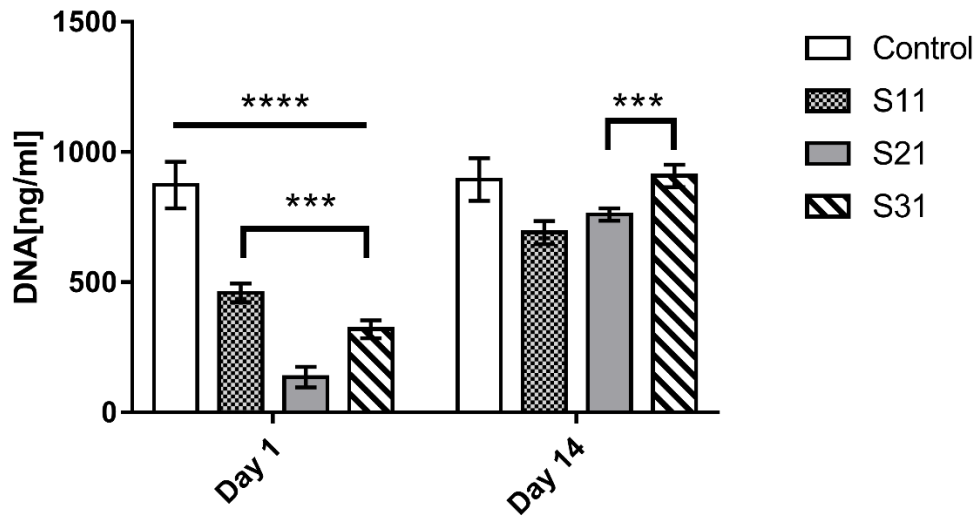
Fig. 7 Cell proliferation of MG-63 cells on pure, binary and ternary doped CHA tested samples were assessed by DNA concentration after 1 and 14 days in comparison with control. Value represent the mean $\pm$ SD of three samples duplicate (*$p \leq 0.05$, **$p \leq 0.01$, ***$p \leq 0.001$ and **** $p \leq 0.0001$). Cells in direct contact with S31 show highest level of DNA after 14 days of culture
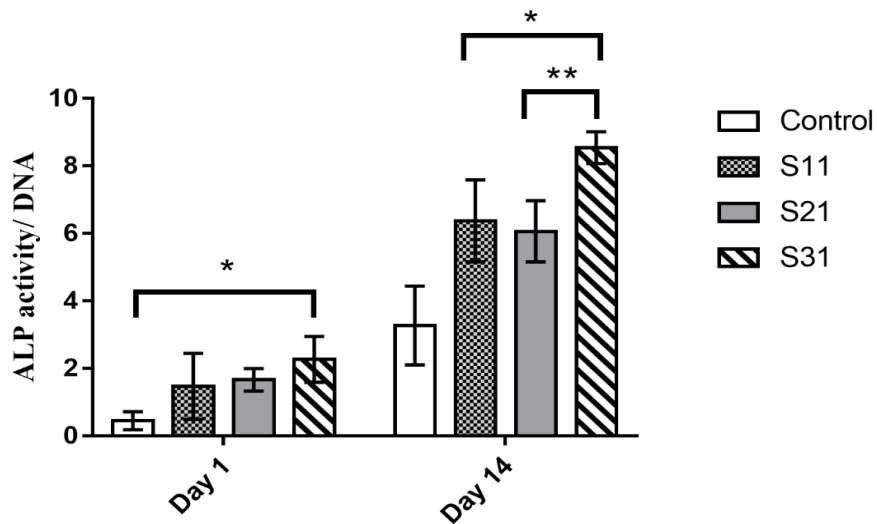

Fig. 8 The level of mean ALP/DNA by MG-63 cells cultured on control, pure, binary and ternary doped CHA tested samples for 1 and 14 days. Value represent the mean $\pm$ SD of three samples duplicate (*$p \leq 0.05$, **$p \leq 0.01$, ***$p \leq 0.001$ and **** $p \leq 0.0001$). Cells in direct contact with S31 show highest level of mean ALP/DNA after 14 days of culture

LIST OF TABLES

Table 1 Compositions of the as-synthesized CHA and multi-doped CHA powders

Sample code	Composition	Molar concentration of reactants (M)					
		Ca^{2+}	PO_4^{3}	CO_3^{2-}	Co^{2+} $(\times 10^{-11})$	Sr^{2+} $(\times 10^{-7})$	Mg^{2+} $(\times 10^{-5})$
S11	CHA				-	-	-
S21	CoSr CHA	0.10	0.06	0.06	2.55	5.67	-
S31	MgCoSr CHA						2.88

Table 2 Crystallographic features of pure, binary and ternary doped CHA sintered scaffolds

Samples	$a=b$ (Å)	c (Å)	Crystallite Size (nm)
HA (#09-0432)	9.418	6.884	-
S11	9.423	6.886	62.670
S21	9.427	6.891	59.370
S31	9.430	6.890	58.930

Table 3 Pore size, porosity and compressive strength of pure, binary and ternary doped CHA scaffolds

Samples	Pore size (mm)	Total porosity (%)	Compressive strength (MPa)
S11	385.60 ± 63.35	89.61	0.50 ± 0.05
S21	327.90 ± 62.97	88.90	0.38 ± 0.04
S31	427.50 ± 54.75	91.93	0.53 ± 0.12